Academic Journal of Applied Sciences
ISSN: 3105-0549 (Print), ISSN: 3105-0557 (Online) | Vol. 1, No. 2, 2026

U-Net-Based Semantic Segmentation and Porosity Analysis of C/GFRP CT Images

Hongzi Xiong, Tao Zeng *

School of Mechanical Engineering, Sichuan University of Science and Engineering, 644004, China

Abstract: Accurate identification of internal voids and clarification of their evolution remain challenging in carbon/glass fiber hybrid composites (C/GFRP). In this study, interlaminar hybrid C/GFRP laminates were investigated using in situ tensile X-ray computed tomography (CT) to perform automatic void segmentation and quantitative analysis. CT images acquired at different loading stages were first preprocessed, and Gaussian, median, and non-local means (NLM) filters were compared, with NLM selected for denoising. Based on a finely annotated manual dataset, a U-Net semantic segmentation model was then established to automatically identify void regions and material-layer structures. On this basis, slice-wise layer-porosity variations along different section directions were analyzed, and the evolution of voids and cracks during loading was investigated in conjunction with three-dimensional reconstruction. The results show that the proposed segmentation workflow can stably identify voids and layer structures in C/GFRP CT images. Dice coefficients of 0.976 and 0.989 were obtained on the validation set for CFRP void segmentation and GFRP layer segmentation, respectively, indicating high accuracy and good generalization. The slice-wise layer porosity exhibits pronounced spatial non-uniformity in different section directions, and high-porosity regions persist during loading and correspond spatially to the final fracture location. Three-dimensional evolution results further reveal a damage process transitioning from dispersed voids to local concentration and then to crack coalescence and propagation. Damage in the GFRP layers propagates significantly faster than in the CFRP layers, indicating that the GFRP layers are the weak region governing progressive failure of the hybrid laminate. These findings provide methodological support for intelligent identification of internal defects, characterization of damage evolution, and correlation analysis of mechanical behavior in C/GFRP composites.

Keywords: C/GFRP, CT, U-Net, void segmentation, layer porosity, damage evolution.

1. Introduction

Fiber-reinforced composites have been widely used in aerospace, rail transit, lightweight automotive structures, and high-end equipment manufacturing because of their high specific strength, high specific stiffness, corrosion resistance, and design flexibility [1]. Compared with single-fiber carbon-fiber-reinforced or glass-fiber-reinforced composites, carbon/glass fiber hybrid composites (C/GFRP) can maintain relatively high load-bearing capacity and structural stiffness while reducing cost, and therefore exhibit considerable engineering potential. During composite manufacturing, insufficient resin flow, non-uniform impregnation, residual volatiles, and improper control of curing pressure and temperature can readily induce mesoscale defects such as voids, dry spots, interfacial debonding, and microcracks [2-4]. In C/GFRP composites, the coexistence of carbon-fiber layers, glass-fiber layers, and complex interfaces makes the formation, distribution, and evolution of voids more complicated than in single-fiber systems. It is therefore necessary to investigate the identification and analysis of internal voids in C/GFRP composites.

Voids are among the most common and most difficult-to-eliminate manufacturing defects in fiber-reinforced composites, and their size, morphology, location, and distribution significantly influence the macroscopic service performance of the material. Little et al. [5] characterized voids in fiber-reinforced composites and pointed out that void morphology and spatial distribution have an important influence on subsequent performance assessment. Bodaghi et al. [6] experimentally characterized void features in composites with high fiber volume fraction. Patou et al. [7] investigated the effects of different compaction processes on voids and mechanical properties in C/PPS laminates and found that process parameters can significantly alter the internal defect state. Tretiak et al. [8] reported that voids reduce the short-beam shear strength of carbon-fiber composites. Wang et al. [9] used acoustic emission and micro-CT to study the damage evolution behavior of carbon-fiber/epoxy composites with different porosity levels. Zhang et al. [10] analyzed the influence of void defects on the impact performance of CFRP laminates using multiscale simulation. These studies indicate that voids not only affect the overall load-bearing capacity of composites but also alter crack initiation, propagation, and final failure modes. In hybrid composites, the role of voids in interlaminar and interfacial regions is even more complex. Jiang et al. [11] used in situ micro-CT to investigate damage evolution in carbon-fiber laminates and carbon/glass hybrid laminates under tensile loading, demonstrating pronounced interlaminar differences in damage propagation within hybrid structures. Wang et al. [12] further combined CT and deep-learning-based identification to quantitatively analyze internal defects in CFRP, GFRP, and C/GFRP laminates, indicating that the integration of CT with intelligent segmentation methods has broad application prospects.

X-ray computed tomography (CT), which can obtain two-dimensional slices and three-dimensional structural information under nondestructive conditions, has become an important technique for characterizing internal defects in composites. Gao et al. [13] showed that CT offers clear advantages in void characterization, damage tracking, and mesoscopic modeling. Naresh et al. [14] argued that CT can be used not only to analyze manufacturing processes for aerospace composites but also to provide basic data for process design and structural modeling. Garcea et al. [15]

systematically summarized CT-based characterization methods for polymer composites and showed that CT can effectively provide mesoscopic information such as void size, morphology, connectivity, and spatial distribution. Rashidi et al. [16] analyzed the challenges associated with optimizing micro-CT characterization of carbon-fiber woven composites. Schilling et al. [17] were among the early researchers to observe internal damage in polymer-matrix composites using X-ray microtomography, thereby verifying the effectiveness of CT for visualization of internal composite defects. Gusenbauer et al. [18] quantitatively measured voids in carbon-fiber- and glass-fiber-reinforced polymers using phase-contrast imaging. Zwanenburg et al. [19] further studied high-quality micro-CT imaging of carbon-fiber composites, and Srivastava et al. [20] performed three-dimensional analysis of voids in glass-fiber/vinyl ester filament-wound composites. Meanwhile, Galvez-Hernandez et al. [21] pointed out that CT scanning parameters directly affect the evaluation of voids in CFRP laminates. These studies indicate that, although CT provides an important means for void identification in composites, image quality and subsequent segmentation strategies remain critical factors affecting the reliability of quantitative results.

Traditional CT image segmentation methods mainly include thresholding, edge detection, region growing, and watershed segmentation. The between-class variance maximization method proposed by Otsu [22] is among the most classical automatic thresholding methods. The edge detector proposed by Canny [23] is representative for boundary extraction. Tilton [24] investigated region-growing segmentation, whereas Levner et al. [25] proposed a classification-driven watershed method. These approaches are conceptually clear and easy to implement, and they can achieve satisfactory results when the grayscale contrast between target and background is sufficiently distinct. However, for composite CT images, the grayscale contrast between voids and the resin matrix is often limited, fiber textures are complex, and noise is substantial. Traditional methods therefore struggle to simultaneously achieve reliable identification of small voids and accurate extraction of their boundaries. Tretiak et al. [26] investigated threshold parameters for void segmentation in composite X-ray CT images and showed that different threshold settings can significantly affect statistical results for porosity, size distribution, and morphology. Accordingly, traditional grayscale-rule-based methods alone are insufficient for stable identification of complex voids in C/GFRP CT images.

With the development of deep learning, semantic segmentation has provided a new technical route for target extraction in complex images. Long et al. [27] proposed the fully convolutional network (FCN), which first enabled end-to-end pixel-level prediction. Ronneberger et al. [28] proposed U-Net, whose encoder-decoder architecture and skip connections achieved excellent performance in medical image segmentation and small-sample tasks. Subsequently, Chen et al. [29] proposed semantic segmentation methods incorporating boundary information, and Chen et al. [30] further improved segmentation performance in DeepLabv3+ by using atrous convolution and an encoder-decoder structure. Zhou et al. [31] proposed UNet++, which further improved feature fusion through dense skip connections. Compared with traditional methods, deep-learning-based segmentation models can automatically learn texture, boundary, and contextual information from images, making them more suitable for CT image segmentation tasks involving low contrast, high noise, and complex backgrounds.

In recent years, deep-learning methods have been increasingly applied to the analysis of composite CT images. Sinchuk et al. [32] combined variational methods with deep learning for segmentation of extremely low-contrast XCT images of carbon/epoxy woven composites. Galvez Hernandez et al. [33] performed phase segmentation of uncured prepregs using X-ray CT images. Zhong et al. [34] used U-Net to segment filamentary targets in fabric micro-CT images. Machado et al. [35] applied machine-learning methods to automatically assess the void content of composite laminates. Badran et al. [36] verified the effectiveness of deep learning in CT image segmentation of fiber-reinforced composites. Helwing et al. [37] used deep learning to analyze and segment fatigue damage in fiber-reinforced polymers. Furthermore, Upadhyay et al. [38] compared deep-learning-based and grayscale-threshold-based methods for void segmentation in filament-wound composites and found that deep learning was superior in characterizing void size, shape, and location. Petkov et al. [39] used Attention U-Net for semantic segmentation of progressive microcracks in polymer composites, and Zheng et al. [40] achieved quantitative characterization of mesoscopic morphological features in damaged woven composites through improved automatic XCT segmentation. Overall, previous studies have laid an important foundation for automatic segmentation of composite CT images; however, integrated studies addressing automatic recognition of void regions, statistics of slice-wise layer porosity, and extraction of morphological features of individual voids in C/GFRP CT images remain limited.

In view of the above, this study takes CT images of C/GFRP composites as the research object. The raw slices were first preprocessed and annotated, after which a U-Net semantic segmentation model was established to automatically identify void regions. On the basis of the segmentation results, slice-wise layer porosity and individual void morphology were further analyzed. The aim of this work is to establish a void identification and quantitative analysis workflow suitable for C/GFRP CT images, thereby providing a foundation for subsequent three-dimensional void reconstruction, defect-evolution analysis, and correlation analysis between void characteristics and mechanical properties.

2. Materials and Methods

2.1. Specimens and Experimental Procedure

The experimental dataset used in this study was previously analyzed using a conventional threshold-based segmentation method in Ref. [11]. The present work focuses on full-image segmentation using deep learning and on the evolution of slice-wise layer porosity. The prepregs used to fabricate the specimens were supplied by Jiangsu Hengshen Co., Ltd. The specific material designations are listed in Table 1.

The specimen dimensions were designed according to the fixture size of the micro-CT testing platform, for which the X-ray scanning field of view was 3 mm × 2.7 mm. An interlaminar hybrid lay-up was adopted. Specifically, CFRP and GFRP plies were stacked in a 2:3:2 ratio, and a symmetric laminate was prepared on the basis of this stacking sequence.

During the tensile experiment, the maximum stress of specimens from the same batch was first obtained through an in situ tensile pretest. Representative characteristic points were then selected as the control nodes for stepwise loading, corresponding to 30%, 60%, and 90% of the maximum stress, together with the initial state and the final fractured state. This loading path was chosen to cover the key mechanical stages from the initial elastic response to damage development. The stress levels corresponding to each CT scan are listed in Table 2.

As shown by the load-displacement curve in Fig. 2, the specimen exhibits an approximately linear mechanical response in the initial loading stage, indicating that the deformation is dominated by elasticity. With increasing displacement, two pronounced fluctuations appear in the middle portion of the curve and are accompanied by local stiffness degradation, suggesting the onset of progressive internal damage. In combination with the subsequent CT observations and fracture-surface analysis, this behavior can be attributed to damage modes such as interfacial debonding, interlaminar delamination, and matrix cracking. Near the final fracture stage, the curve deviates markedly from the initial linear path and then rapidly drops to zero, indicating that significant damage accumulation and structural instability occurred before ultimate failure. Overall, the hybrid laminate exhibits a typical progressive damage response under tensile loading.

Table 1. Prepreg materials used in the specimens

Composite	Model	Fiber content
CFRP	EM119-45%-3KHF10-200gsm-1000	45%
GFRP	EM119-42%-EWR200-200gsm-1000	42%

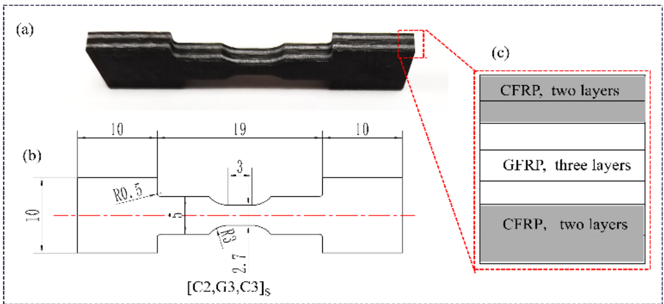

Figure 1. Lay-up of the specimen

Table 2. Stress levels corresponding to CT scans

CT scan point	Initial state	0.3 stage	0.6 stage	0.9 stage	Fracture state
[C2, G3, C2]s	0 MPa	142 MPa	283 MPa	425 MPa	-

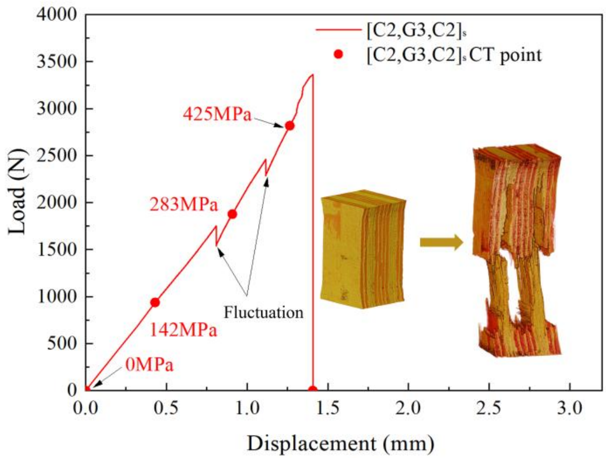

Figure 2. Load-displacement curve of the specimen

2.2. Image Preprocessing and Dataset Preparation

Filtering is a key step in image analysis because it directly affects the accuracy and reliability of subsequent quantitative analysis. To balance computational efficiency and segmentation accuracy, a volume of interest (VOI) of 894 × 969 × 1283 voxels was extracted from the middle region of the specimen for detailed analysis of the internal microstructure. The selected VOI was located near a damage-prone region and was therefore considered representative of the material's internal microstructural features.

Gaussian filtering, median filtering, and non-local means (NLM) filtering were applied to denoise the CT images of the [C2, G3, C2]s specimen. For Gaussian filtering, the kernel mode was set to separable, the kernel size was set to 2, and both x and y values were set to 1. For median filtering, the window size was set to 4 × 4. For NLM filtering, the spatial standard deviation was set to 5, the intensity standard deviation to 0.2, the search region to 4 × 4, and the number of neighborhood pixels to 3. The processed results are shown in Figs. 3 and 4.

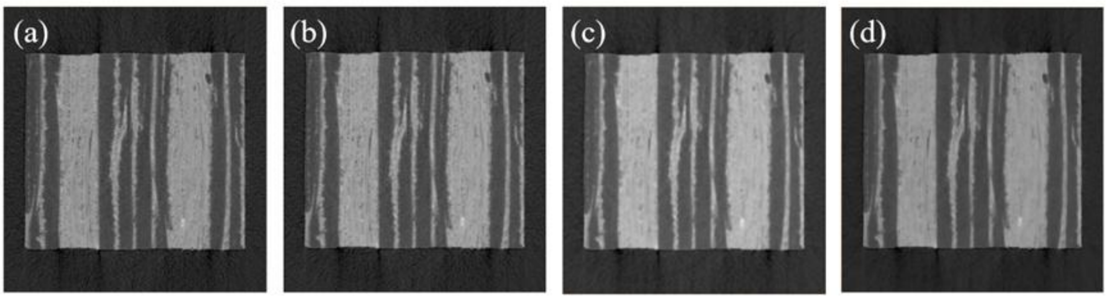

Figure 3. Slice images after different filtering methods: (a) original image; (b) Gaussian filtering; (c) median filtering; (d) non-local means filtering

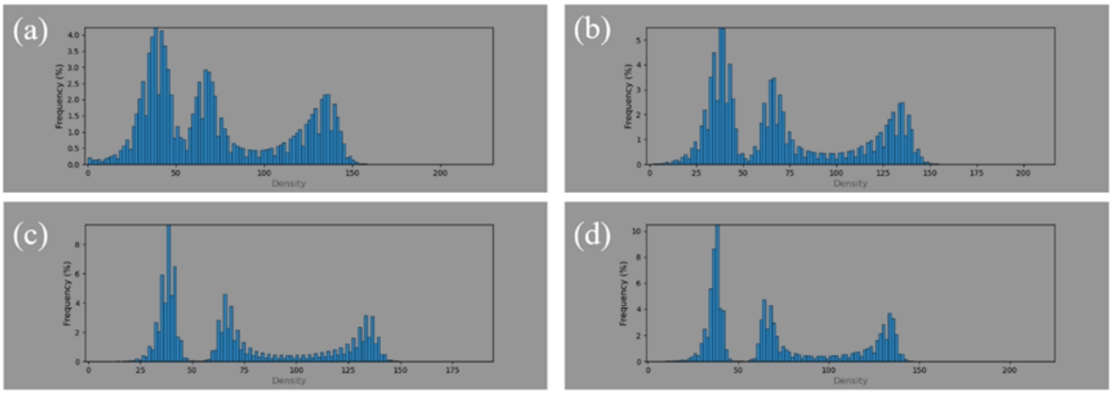

Figure 4. Grayscale distribution of [C2, G3, C2]s under different filtering methods: (a) original image; (b) Gaussian filtering; (c) median filtering; (d) non-local means filtering

Table 3. Comparison of evaluation metrics for the three filtering methods

Method	MSE	SSIM	PSNR
Gaussian filtering	2.42	0.947414	44.28
Median filtering	15.85	0.678662	36.129
NLM	7.9	0.771919	39.156

Table 3 summarizes the objective evaluation metrics of the three filtering methods. Considering both the objective metrics and the subjective visual quality, Gaussian filtering performs well according to the numerical indicators but tends to smooth local edges and fine structures, which may lead to ghosting and local deformation. Median filtering preserves low-gray-value regions that are close to the original image; however, it easily causes overall blurring and substantial loss of fine details, which is unfavorable for subsequent fine segmentation. Compared with the previous two methods, NLM yields slightly lower MSE, SSIM, and PSNR values than Gaussian filtering, but it shows a better overall balance in preserving structural boundaries, retaining fine textures, and distinguishing between high- and low-gray-value regions. NLM can improve the separability among different constituents while preserving important image textures and distribution features more completely, which better satisfies the practical requirements of subsequent component segmentation in terms of realism and detail retention. Therefore, NLM was selected as the image-filtering method in the remainder of this study.

All datasets were annotated and partitioned on the Avizo platform. Initial labels were generated by Avizo semi-automatic segmentation and then manually refined slice by slice on representative images. After repeated verification, the labels were used for network training and validation. During annotation, membrane enhancement filtering was first applied to strengthen the boundary structures of different components and improve the grayscale contrast between voids and the matrix. Void features were then extracted by combining interactive threshold segmentation and interactive top-hat segmentation.

A coarse-to-fine void extraction strategy, progressing from large to small defects, was adopted to match the multiscale nature of internal defects in the C/GFRP specimen. Large voids with pronounced grayscale contrast and clear morphological features were first extracted by interactive threshold segmentation. On this basis, interactive top-hat segmentation was used to supplement and screen small defects. The specific procedure is illustrated in Fig. 5. This workflow enables accurate identification of large voids while also maintaining good sensitivity to fine voids, thus providing reliable data for subsequent calculations of porosity, void-size distribution, and spatial clustering characteristics.

Representative labeling results are shown in Fig. 6. A total of 100 representative slices were ultimately selected and manually annotated as the initial dataset for model training. After annotation, the labeled two-dimensional slices were augmented by mirror flipping, rotation, and scale transformation to alleviate overfitting and limited generalization in small-sample training. Finally, the augmented dataset was randomly divided into a training set and a validation set at a ratio of 8:2. The validation set was used as an independent basis for evaluating segmentation accuracy, convergence stability, and generalization ability.

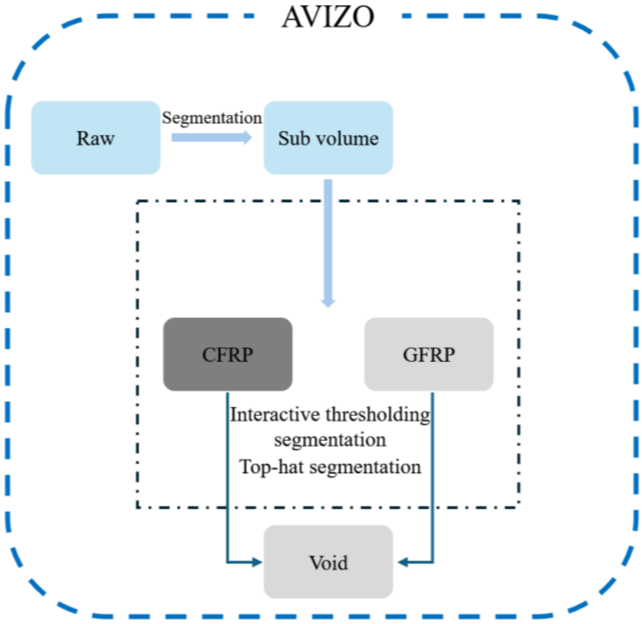

Figure 5. Schematic diagram of dataset labeling

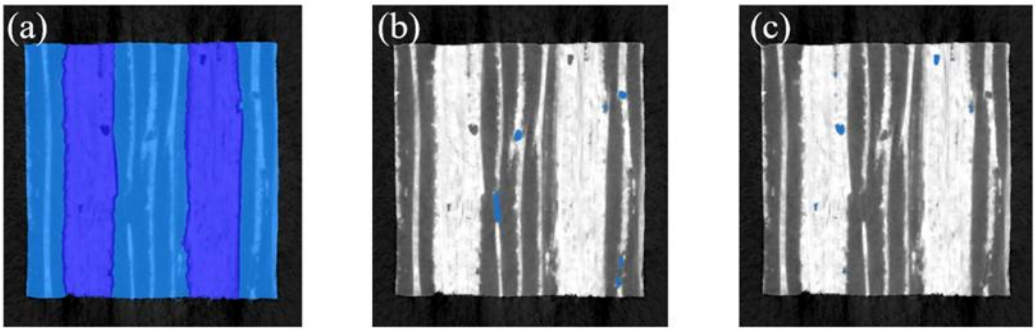

Figure 6. Examples of dataset labeling: (a) discrimination of different regions; (b) void labels in the CFRP region; (c) void labels in the GFRP region

2.3. U-Net Architecture and Training Strategy

All model training was conducted on the Dragonfly software platform. The training parameters were set as follows: patch size = 256 × 256 pixels, input stride ratio = 0.3, initial learning rate = 0.0001, and number of training epochs = 400. Under this unified training strategy, the segmentation models were trained and then applied to the image segmentation tasks at the corresponding loading stages. The overall workflow is shown in Fig. 7.

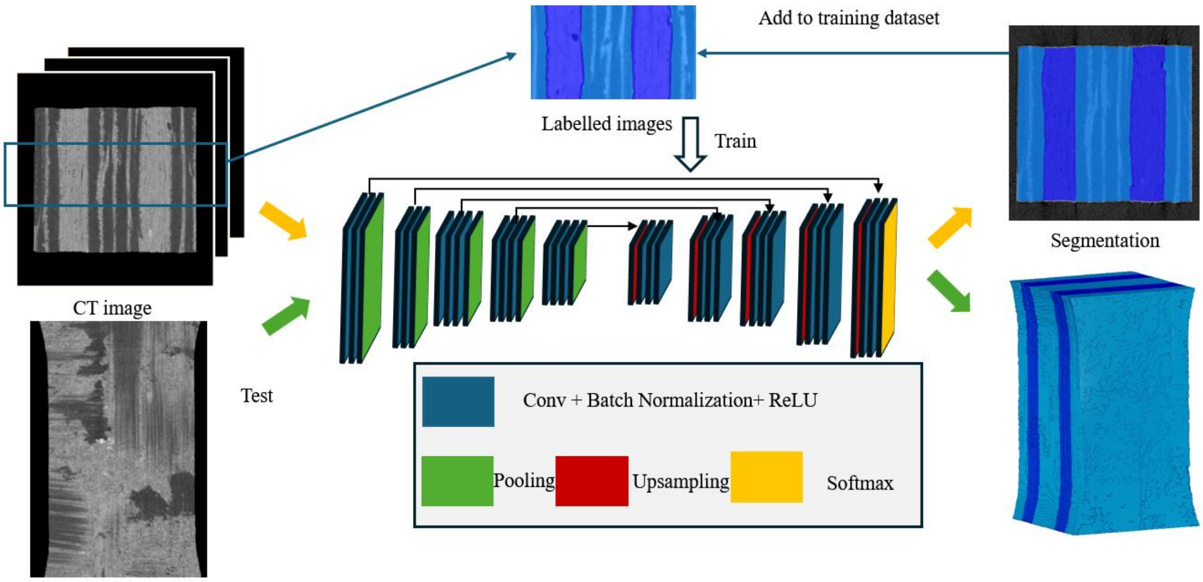

Figure 7. Schematic workflow of deep-learning-based training

Through the above standardized data augmentation, network construction, and training strategy, a high-accuracy segmentation model for the multiphase microstructure of the composite was obtained. To illustrate the convergence behavior during training, two representative training results were selected, and the corresponding loss functions and Dice-coefficient curves are shown in Fig. 8.

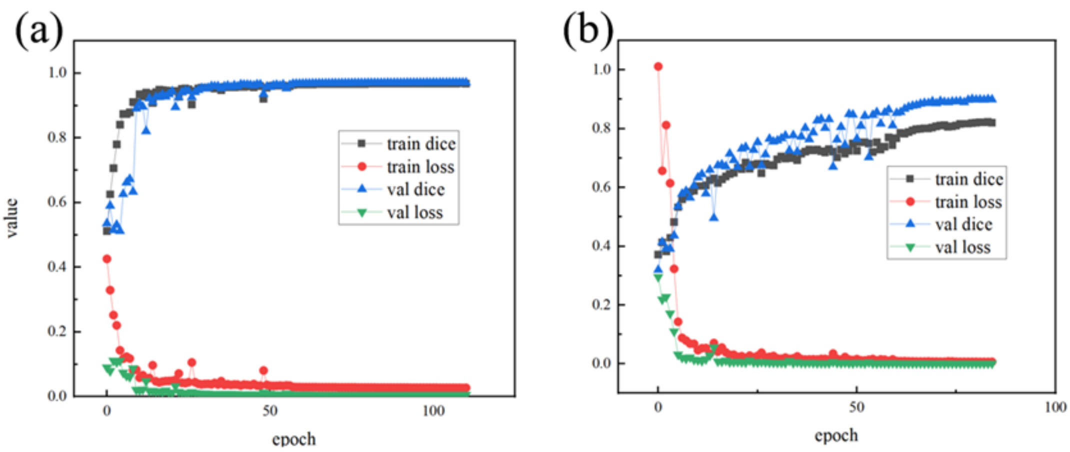

Figure 8. Training loss and Dice coefficient: (a) CFRP void segmentation; (b) GFRP layer segmentation

Figure 8(a) shows that the model for CFRP void segmentation converges rapidly in the early iterations and then enters a relatively stable fine-optimization stage. During the initial iterations, the model successfully captures the primary features of the void regions, and the Dice coefficient of the validation set increases from 0.685 to 0.976 while the loss function decreases synchronously, indicating that the U-Net model can effectively learn the main morphological features and spatial distribution of dispersed voids. In the subsequent refinement stage, the performance-gain curve gradually flattens and reaches a high-level plateau, while the loss is further reduced to the order of 0.005 with markedly narrowed fluctuations. This indicates that the later training stage mainly focuses on refining void-boundary details and suppressing noise interference. Although the validation curve exhibits slight oscillations at the beginning, this can be attributed to the small scale of the target voids and the sensitivity of gradient updates under a low signal-to-noise ratio. As training proceeds, however, the curve converges and stabilizes at a high level of 0.976. Throughout the process, the training and validation metrics remain highly consistent, and no signs of overfitting such as increasing validation loss or deteriorating accuracy are observed, indicating good convergence stability and generalization ability under the present dataset conditions.

Compared with void segmentation, the GFRP-layer segmentation model in Fig. 8(b) exhibits a faster convergence rate at the initial stage. This may be because GFRP layers in CT images typically appear as regions with relatively high grayscale values, higher uniformity, and stronger continuity, so most of the segmentation task can be completed well at an early stage of training. The Dice coefficient rises to 0.989 within a relatively small number of iterations, and the loss then steadily decreases to 0.002 as training proceeds. During the subsequent optimization stage, the curves vary slowly with only minor fluctuations, and the training and validation curves almost overlap throughout the entire process, indicating that no overfitting occurs. Compared with void segmentation, the GFRP-layer segmentation task exhibits more stable convergence and enables more robust extraction of the relevant features for accurate segmentation.

Taken together, the loss and Dice-coefficient curves for the two segmentation tasks indicate that both void segmentation and layer segmentation are characterized by rapid early convergence followed by stabilization at later stages. Nevertheless, differences still exist in convergence speed, final accuracy, and curve fluctuation, which are mainly attributable to differences in the spatial morphology, scale, and grayscale distribution of the segmentation targets.

3. Results

3.1. Results of Slice-wise Layer Porosity Analysis

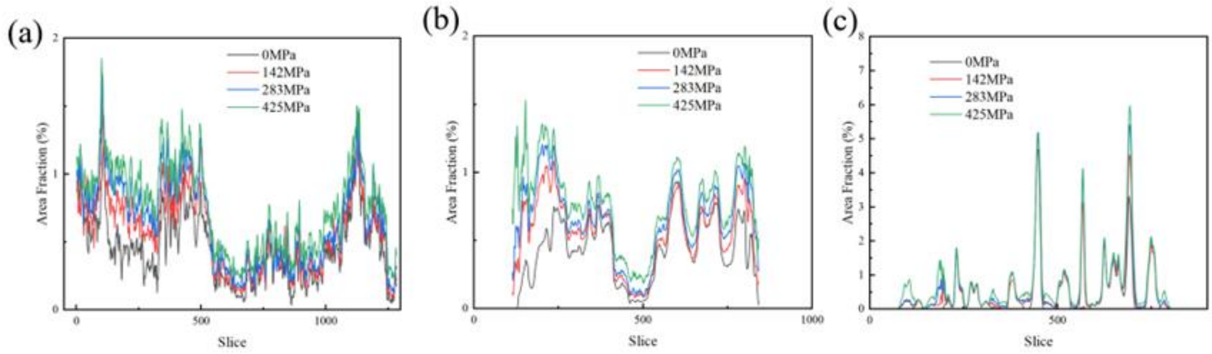

Figure 9. Slice-wise layer-porosity variation of [C2, G3, C2]s at different loading stages: (a) XY planes; (b) XZ planes; (c) YZ planes

As shown in Fig. 9(a), the slice-wise layer porosity along the Z direction is not uniform along the specimen length, and the curve does not exhibit an obvious regular pattern. This is mainly because the initial differences originate from inherent defects formed during specimen manufacturing. It can also be observed that slices with higher initial porosity experience more pronounced porosity variation during the experiment. Moreover, the slice corresponding to the peak layer porosity shows a certain spatial correspondence with the final fracture location, indicating that the distribution of initial defects can influence the site of damage initiation to some extent.

Figure 9(b) shows that the layer porosity of the XZ planes along the Y direction is likewise markedly non-uniform, with large differences among slices and no simple periodic trend overall. This suggests that the spatial distribution of voids in the XZ planes is still mainly governed by initial defects generated during manufacturing, and that obvious local enrichment exists at different positions. From the shapes of the curves, the locations of porosity peaks and valleys remain largely consistent along the slice direction under different stress levels, indicating that the high- and low-porosity regions exhibit clear spatial persistence. In other words, the initial defect distribution plays a dominant role in subsequent damage evolution.

As shown in Fig. 9(c), the layer porosity of the YZ planes along the X direction also exhibits pronounced non-uniformity and strong fluctuations along the slice direction. However, compared with the XY and XZ planes, the variation is more characterized by local abrupt increases: most slices maintain relatively low layer porosity, whereas only a few specific locations show obvious sharp peaks. This indicates that void distribution in the YZ planes is highly localized, with voids concentrated in several discrete regions rather than being continuously and uniformly distributed along the specimen length. The phenomenon further suggests that the internal defect distribution in this direction is strongly random and mainly originates from initial voids and local defect clustering formed during manufacturing.

3.2. Three-Dimensional Evolution of Internal Voids

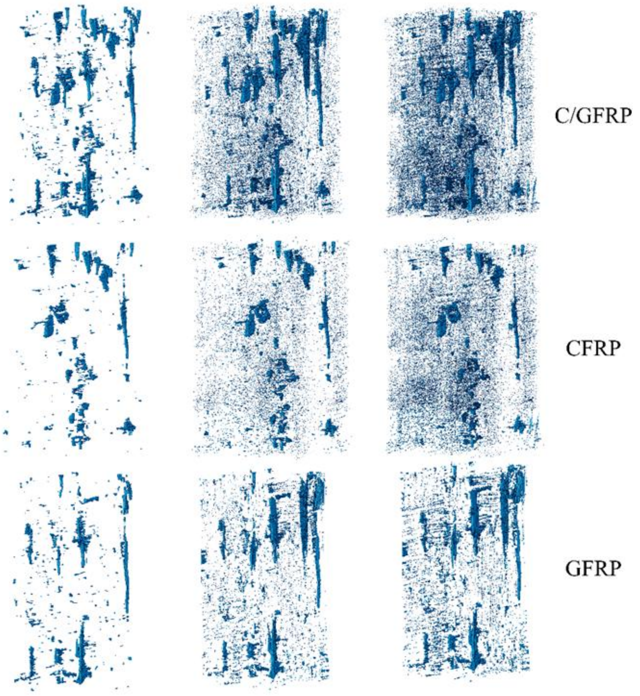

Figure 10. Three-dimensional reconstruction of void evolution under different load levels

Figure 10 presents the three-dimensional evolution of internal voids in the entire specimen as well as in the CFRP and GFRP layers during the CT scanning experiment. The evolution of the defects reveals the full process of microcrack initiation, propagation, and eventual coalescence inside the specimen. The different evolution patterns observed in the two reinforcing-fiber layers indicate that the final failure behavior is jointly influenced by the material properties of the two fiber systems and by the interfacial state between adjacent layers.

In the initial state, a certain number of manufacturing-induced defects are already present inside the specimen, mainly in the form of dispersed microvoids and short cracks distributed within the CFRP and GFRP layers. Defects in the CFRP layers are relatively uniformly distributed, and the structural integrity remains comparatively good. By contrast, the void distribution in the GFRP layers is more irregular, and local cracks are longer. As the stress increases, the internal defects gradually evolve from a dispersed distribution toward local concentration, and several defect-enriched zones form along the longitudinal direction. This indicates continued damage development near the hybrid interfaces, while stress redistribution among the constituents further promotes interfacial debonding and the coalescence and propagation of microcracks.

From the viewpoint of the different reinforcing-fiber layers, only a small number of new microcracks are generated in the CFRP layers during the test, and the growth of manufacturing-induced initial voids remains relatively slow, so the overall structural integrity is largely preserved. In contrast, crack propagation in the GFRP layers is much more pronounced, and in some local regions the internal damage approaches through-thickness connectivity. When the stress reaches 425 MPa, the internal damage becomes clearly concentrated in the GFRP layers, where a relatively dense crack network forms between adjacent GFRP regions. This produces an obvious damage-concentration band in the upper part of the specimen. At this stage, the CFRP layers are still dominated by isolated voids and do not yet contain cracks penetrating the specimen, whereas the GFRP layers have already developed multiple parallel cracks together with a distinct longitudinal main crack.

Combined with the observed internal defect evolution during the experiment, it can be inferred that the higher elastic modulus of the CFRP layers allows them to play a stronger constraining and load-bearing role, thereby reducing excessive local stress concentration and slowing the evolution of internal damage. Because the GFRP layers have lower stiffness, local deformation concentration and crack growth are more likely to occur at the interfaces between the two reinforcing fibers and around void edges. In the C/GFRP hybrid system, early damage in the GFRP layers can further affect neighboring CFRP layers through interface interactions, aggravate local stress concentration, and trigger subsequent cracking, ultimately leading to overall specimen failure.

4. Conclusions

(1) By combining NLM filtering, enhanced manual annotation, and U-Net semantic segmentation, stable identification of void regions and interlaminar structures was achieved. Dice coefficients of 0.976 and 0.989 were obtained on the validation set for CFRP void segmentation and GFRP layer segmentation, respectively, demonstrating good convergence and generalization of the model.

(2) The C/GFRP specimen exhibits pronounced spatial non-uniformity in slice-wise layer porosity along different section directions, and high-porosity regions show clear spatial persistence during loading. Regions with higher initial porosity undergo more severe changes during subsequent loading and show a certain spatial correspondence with the final fracture location, indicating that initial defects formed during manufacturing play a dominant role in damage initiation and propagation.

(3) Three-dimensional reconstruction shows that internal damage in C/GFRP evolves during tensile loading from dispersed voids to local concentration and then to crack coalescence and through-thickness development. Damage propagates significantly faster in the GFRP layers than in the CFRP layers; at 425 MPa, the GFRP layers have already formed a relatively dense crack network while the CFRP layers largely maintain their integrity, indicating that the GFRP layers and their interfacial regions are the weak links governing progressive failure of the hybrid laminate.

Acknowledgment

The Innovation Fund of Postgraduate, Sichuan University of Science & Engineering (Y2024008)

References

[1] Rajak D K, Pagar D D, Menezes P L, et al. Fiber-Reinforced Polymer Composites: Manufacturing, Properties, and Applications [J]. Polymers, 2019, 11(10): 1667.

[2] Mehdikhani M, Gorbatikh L, Verpoest I, et al. Voids in fiber-reinforced polymer composites: A review on their formation, characteristics, and effects on mechanical performance [J]. Journal of Composite Materials, 2019, 53(12): 1579-1669.

[3] Dong C. Effects of Process-Induced Voids on the Properties of Fibre Reinforced Composites [J]. Journal of Materials Science & Technology, 2016, 32(7): 597-604.

[4] Liu X, Chen F. A review of void formation and its effects on the mechanical performance of carbon fiber reinforced plastic [J]. Engineering Transactions, 2016, 64(1): 33-51.

[5] Little J E, Yuan X, Jones M I. Characterisation of voids in fibre reinforced composite materials [J]. NDT & E International, 2012, 46: 122-127.

[6] Bodaghi M, Cristóvão C, Gomes R, et al. Experimental characterization of voids in high fibre volume fraction composites processed by high injection pressure RTM [J]. Composites Part A: Applied Science and Manufacturing, 2016, 82: 88-99.

[7] Patou J, Bonnaire R, De Luycker E, et al. Influence of consolidation process on voids and mechanical properties of powdered and commingled carbon/PPS laminates [J]. Composites Part A: Applied Science and Manufacturing, 2019, 117: 260-275.

[8] Tretiak I, Hallett S R. Predicting short beam shear strength reduction in carbon fibre composites containing voids [J]. Composite Structures, 2022, 290: 115472.

[9] Wang J, Zhou W, Wei Z Y, et al. Effects of various porosities on the damage evolution behavior of carbon fiber/epoxy composites using acoustic emission and micro-CT [J]. Journal of Composite Materials, 2022, 56(10): 1507-1524.

[10] Zhang J, Xie J, Zhao X, et al. Influence of void defects on impact properties of CFRP laminates based on multi-scale simulation method [J]. International Journal of Impact Engineering, 2023, 180: 104706.

[11] Jiang L, Xiong H, Zeng T, et al. In-situ micro-CT damage analysis of carbon and carbon/glass hybrid laminates under tensile loading by image reconstruction and DVC technology [J]. Composites Part A: Applied Science and Manufacturing, 2024, 176: 107844.

[12] Wang M, Zhang B, Zhan S, et al. Micro-Computed Tomography Non-Destructive Testing and Defect Quantitative Analysis of Carbon Fiber-Reinforced Polymer, Glass Fiber-Reinforced Polymer and Carbon/Glass Hybrid Laminates Using Deep Learning Recognition [J]. Applied Sciences, 2025, 15(22): 12192.

[13] Gao Y, Hu W, Xin S, et al. A review of applications of CT imaging on fiber reinforced composites [J]. Journal of Composite Materials, 2022, 56(1): 133-164.

[14] Naresh K, Khan K A, Umer R, et al. The use of X-ray computed tomography for design and process modeling of aerospace composites: A review [J]. Materials & Design, 2020, 190: 108553.

[15] Garcea S C, Wang Y, Withers P J. X-ray computed tomography of polymer composites [J]. Composites Science and Technology, 2018, 156: 305-319.

[16] Rashidi A, Olfatbakhsh T, Crawford B, et al. A Review of Current Challenges and Case Study toward Optimizing Micro-Computed X-Ray Tomography of Carbon Fabric Composites [J]. Materials, 2020, 13(16): 3606.

[17] Schilling P J, Karedla B P R, Tatiparthi A K, et al. X-ray computed microtomography of internal damage in fiber reinforced polymer matrix composites [J]. Composites Science and Technology, 2005, 65(14): 2071-2078.

[18] Gusenbauer C, Reiter M, Plank B, et al. Porosity Determination of Carbon and Glass Fibre Reinforced Polymers Using Phase-Contrast Imaging [J]. Journal of Nondestructive Evaluation, 2019, 38: 1.

[19] Zwanenburg E A, Norman D G, Qian C, et al. Effective X-ray micro computed tomography imaging of carbon fibre composites [J]. Composites Part B: Engineering, 2023, 258: 110707.

[20] Srivastava C, Agostino P, Stamopoulos A G, et al. Three-Dimensional Analysis of Porosity in As-Manufactured Glass Fiber/Vinyl Ester Filament Winded Composites Using X-Ray Micro-Computed Tomography [J]. Applied Composite Materials, 2024, 31: 171-200.

[21] Galvez-Hernandez P, Smith R A, Gaska K, et al. The effect of X-ray computed tomography scan parameters on porosity assessment of carbon fibre reinforced plastics laminates [J]. Journal of Composite Materials, 2023, 57(29): 4535-4548.

[22] Otsu N. A Threshold Selection Method from Gray-Level Histograms [J]. IEEE Transactions on Systems, Man, and Cybernetics, 1979, 9(1): 62-66.

[23] Canny J. A Computational Approach to Edge Detection [J]. IEEE Transactions on Pattern Analysis and Machine Intelligence, 1986, 8(6): 679-698.

[24] Tilton J C. Image Segmentation by Region Growing and Spectral Clustering with a Natural Convergence Criterion [C]//Proceedings of IGARSS 1998. Seattle, 1998.

[25] Levner I, Zhang H. Classification-driven watershed segmentation [J]. IEEE Transactions on Image Processing, 2007, 16(5): 1437-1445.

[26] Tretiak I, Smith R A. A parametric study of segmentation thresholds for X-ray CT porosity characterisation in composite materials [J]. Composites Part A: Applied Science and Manufacturing, 2019, 123: 10-19.

[27] Long J, Shelhamer E, Darrell T. Fully Convolutional Networks for Semantic Segmentation [C]//2015 IEEE Conference on Computer Vision and Pattern Recognition. Boston, 2015: 3431-3440.

[28] Ronneberger O, Fischer P, Brox T. U-Net: Convolutional Networks for Biomedical Image Segmentation [C]//Medical Image Computing and Computer-Assisted Intervention – MICCAI 2015. Cham: Springer, 2015: 234-241.

[29] Chen L C, Barron J T, Papandreou G, et al. Semantic Image Segmentation with Task-Specific Edge Detection Using CNNs and a Discriminatively Trained Domain Transform [C]//2016 IEEE Conference on Computer Vision and Pattern Recognition. Las Vegas, 2016: 4545-4554.

[30] Chen L C, Zhu Y, Papandreou G, et al. Encoder-Decoder with Atrous Separable Convolution for Semantic Image Segmentation [C]//Computer Vision – ECCV 2018. Cham: Springer, 2018: 833-851.

[31] Zhou Z, Siddiquee M M R, Tajbakhsh N, et al. UNet++: A Nested U-Net Architecture for Medical Image Segmentation [C]//Deep Learning in Medical Image Analysis and Multimodal Learning for Clinical Decision Support. Cham: Springer, 2018: 3-11.

[32] Sinchuk Y, Kibleur P, Aelterman J, et al. Variational and Deep Learning Segmentation of Very-Low-Contrast X-ray Computed Tomography Images of Carbon/Epoxy Woven Composites [J]. Materials, 2020, 13(4): 936.

[33] Galvez Hernandez P, Gaska K, Kratz J. Phase segmentation of uncured prepreg X-Ray CT micrographs [J]. Composites Part A: Applied Science and Manufacturing, 2021, 149: 106527.

[34] Zhong Q, Zhang J, Xu Y, et al. Filamentous target segmentation of weft micro-CT image based on U-Net [J]. Micron, 2021, 146: 103072.

[35] Machado J M, Tavares J M R S, Camanho P P, et al. Automatic void content assessment of composite laminates using a

machine-learning approach [J]. Composite Structures, 2022, 288: 115383.

[36] Badran A, Parkinson D, Ushizima D, et al. Validation of Deep Learning Segmentation of CT Images of Fiber-Reinforced Composites [J]. Journal of Composites Science, 2022, 6(2): 60.

[37] Helwing R, Hülsbusch D, Walther F. Deep learning method for analysis and segmentation of fatigue damage in X-ray computed tomography data for fiber-reinforced polymers [J]. Composites Science and Technology, 2022, 230: 109781.

[38] Upadhyay S, George Smith A, Vandepitte D, et al. Deep-learning versus greyscale segmentation of voids in X-ray computed tomography images of filament-wound composites [J]. Composites Part A: Applied Science and Manufacturing, 2024, 177: 107937.

[39] Petkov V I, Pakkam Gabriel V R, Fernberg P. Semantic segmentation of progressive micro-cracking in polymer composites using Attention U-Net architecture [J]. Tomography of Materials and Structures, 2024, 5: 100028.

[40] Zheng K, Cao X, Jiang Z, et al. Improved XCT image automatic segmentation for quantitative characterization of the meso-morphological features in the damaged braided composite fabric [J]. Composites Science and Technology, 2024, 247: 110395.